INTERNATIONAL JOURNAL FOR NUMERICAL METHODS IN ENGINEERING
Int. J. Numer. Meth. Engng 2016; **00**:1–25
Published online in Wiley Online Library (wileyonlinelibrary.com). DOI: 10.1002/nme

Enhanced Mesoscale Partitioned Modelling of Heterogeneous Masonry Structures

E. Minga*†, L. Macorini, B. A. Izzuddin

Department of Civil and Environmental Engineering, Imperial College London, SW7 2AZ, UK.

SUMMARY

This paper presents an accurate and efficient computational strategy for the 3D simulation of heterogeneous structures with unreinforced masonry (URM) components. A mesoscale modelling approach is employed for the URM parts, while other material components are modelled independently with continuous meshes. The generally non-matching meshes of the distinct domains are coupled with the use of a mesh tying method. The physical interaction between the components is captured with the use of zero-thickness cohesive interface elements. This strategy enables the optimisation of the individual meshes leading to increased computational efficiency. Furthermore, the elimination of the mesh compatibility requirement allows the 3D modelling of complex heterogeneous structures, ensuring the accurate representation of each component's nonlinear behaviour and their interaction. Numerical examples, including a comparative analysis on the elastic and nonlinear response of a masonry bridge considering arch-backfill interaction and the nonlinear simulation of a multi-leaf wall, are presented to show the unique features of the proposed strategy as well as its predictive power in comparison with experimental and numerical results found in the literature. Copyright © 2016 John Wiley & Sons, Ltd.

Received . . .

KEY WORDS: heterogeneous structures, nonlinear analysis, mesoscale masonry model, mesh tying, coupling element

1. INTRODUCTION

The accurate modelling of masonry is important for both the design of new structures and the assessment of existing ones, a large number of which are still in use. In general, URM presents a complex anisotropic behaviour due to the interaction among the different constitutive components. The mechanical response at the structural scale depends on the properties of each constituent and is strongly connected to the mesostructure of the material. As a result, the development of accurate numerical models for the prediction of the response of masonry structures with arbitrary geometry in 3D remains a major challenge.

For various real problems, URM is coupled with other materials forming heterogeneous structures. In these cases, the interaction between components made of different materials has a significant influence on the failure modes and the ultimate load capacity of the coupled system. Some characteristic examples are masonry arches interacting with backfill material, multi-leaf walls or retrofitted URM components. In such cases, the investigation of the structural response requires the realistic modelling of the interaction between the individual structural parts, as sliding and/or separation might occur along the coupling interfaces.

*Correspondence to: Skempton Building, Department of Civil and Environmental Engineering, South Kensington Campus, Imperial College London, SW7 2AZ, UK.
†email:e.minga13@imperial.ac.uk

In the past, simplified approaches have been employed to predict the response of heterogeneous masonry structures. Masonry arch bridges have been assessed based on kinematic analysis and semi-empirical rules [1]. In the case of multi-leaf walls, analytical relations have been proposed based on a limited number of experimental data available [2]. Obviously, these 2D phenomenological approaches do not account for all the parameters that can influence the response of a heterogeneous structure, hence they offer a restricted level of accuracy and reliability.

For a more generic and accurate estimation of the failure modes and the ultimate load capacity of coupled masonry structures, limit analysis has been extensively used [3, 4, 5, 6]. The URM parts have been modelled with varying levels of detail, starting from simplified 2D representations using beam elements with concentrated plasticity [3]. In more sophisticated descriptions, homogenisation techniques have been applied [5], in an attempt to represent the effect of the mesostructure. Finally, a 3D description which explicitly takes into account the mesostructure of the material has been employed in [6]. In all cases, rigid perfect-plastic interface elements are used to simulate the coupling between structural parts. Those approaches, although efficient for predicting the ultimate capacity of the structure, still do not provide a complete description of the nonlinear response.

In order to predict the nonlinear response of fully coupled structures, previous works have employed 2D and 3D finite element models [5, 7, 8, 9, 10] often using commercial software. In most cases, masonry is modelled macroscopically using anisotropic constitutive laws [5, 7, 8, 9], though simplified descriptions with isotropic material behaviour also exist [10]. The macroscopic description facilitates the coupling with the non-masonry domain and reduces the computational cost. However, it might fail to provide a realistic representation of the failure modes in 3D and the identification of the material model parameters is not straightforward, especially when commercial software models - not specifically designed for masonry - are employed.

A few more refined FE models have been developed specifically for the case of arch bridges with backfill material. A 2D model with unilateral contact elements for the dry joints of the arch and for the interface between arch and backfill has been tested by Betti et al. [11] with interesting results. A similar FE approach with cohesive interface elements instead of contact has been employed by Thavalingam et al. [12] and compared to 2D discontinuous modelling approaches, highlighting the import role of the interaction between the arch and backfill domains. Milani et al. [13] developed a 3D description for arch bridges with simple 3-spring interfaces for the potential failure surfaces. In [14] a mesoscale approach with cohesive interface elements has been employed for the 3D simulation of the arch, while the backfill is modelled with a Mohr-Coulomb type material. The last two types of model take into account the bonding pattern of the arch in 3D and allow the investigation of transversal effects and asymmetric loading. However, the coupling of the different structural parts is achieved through interface elements and requires mesh compatibility along the interface which is impractical or even impossible to achieve in more complex heterogeneous structures.

Based on the above considerations, this paper proposes a novel computational strategy for coupled masonry structures with the following features: i) 3D description of the coupled structure, ii) accurate and sufficiently generic representation of the nonlinear behavior of masonry components, iii) realistic description of the interaction between the components in small and large deformations, including the possibility of sliding, iv) flexible coupling scheme, applicable to different types of heterogeneous structures and v) reduced computational time required for the nonlinear analysis of the complete models.

In this strategy, URM components are simulated with the 3D mesoscale model proposed in [15]. The model accounts for both geometric and material nonlinearity and can accurately predict the nonlinear response of masonry components with arbitrary regular bonding patterns subjected to in- and out-of-plane loading. The increased computational cost generally linked to the 3D mesoscale description of URM is efficiently addressed by the use of a domain partitioning method [16, 17]. Any other material component - e.g. the backfill in masonry bridges - is modelled individually. The resulting generally non-conforming interface between the masonry and the adjacent material is treated with i) one layer of zero thickness cohesive interface elements, reflecting the physical behaviour of the interface with the possibility of sliding and crack opening and ii) a mesh tying

DOI: 10.1002/nme

technique which rigidly connects the non-matching sides of the interface. The mesh tying is achieved with the use of a coupling finite element that has been developed for this purpose. The basic element is founded on a standard 3D two-field mortar method while a variant with penalty stabilisation has also been developed. The formulation of the coupling element is described in Section 3. The performance of the element regarding the accurate transmission of displacement and stress fields between the coupled domains - that has a critical influence to the accuracy of the proposed modelling strategy - is also examined.

The computational strategy introduced here ensures significant flexibility in the meshing of the individual parts of a structure, allowing the modelling of complex heterogeneous systems which might include both mesoscale and macroscale representations of different components. Furthermore, the independence of the domains offers the possibility to reduce the number of elements of the secondary structural components which results in significant speed-up of the analysis.

In the following, some details about the mesoscale masonry model and the domain partitioning framework are provided in Section 2. In Section 3, the main features of the interface coupling element and some details on its implementation are described and standard numerical tests are presented for the validation of its performance. Subsequently, the proposed computational strategy is schematically outlined. Finally, numerical examples and comparisons with available experimental data are presented in Section 4 to demonstrate the potential of the approach for the mesoscale modelling of coupled structural systems with non-conforming interfaces.

2. PARTITIONED MESOSCALE MASONRY MODELLING

2.1. Mesoscale masonry model

The mesoscale model used for representing the nonlinear behaviour of URM [15] combines 3D elastic continuum solid elements for the discretisation of the blocks with 2D nonlinear interface elements, representing the mortar and block-mortar interfaces in a unified way. In addition, the possibility of block failure in tension and shear is taken into account by arranging zero-thickness interface elements within blocks at the level of intersecting head joints [15], as shown in Figure 1.

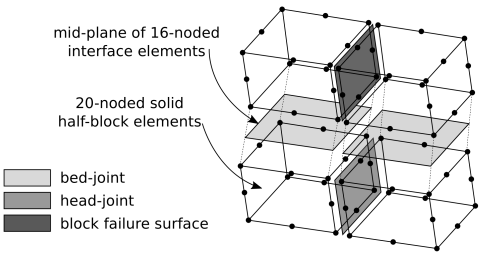

Figure 1. Mesoscale description of masonry.

While the 20-noded brick-elements employ a standard linear elastic material model based on Green's strain, the 16-noded interface elements account for both geometric and material nonlinearity. The possibility of large displacements is considered in the interface elements with the use of a co-rotational approach [18]. The material nonlinearity is taken into account with a multi-surface elastoplastic constitutive model, as illustrated in Figure 2(a). In the elastic region, the normal stiffness k_n and the stiffness in shear k_t are decoupled and their individual values are defined as functions of the elastic properties of the joint material and of the joint dimensions. The post-elastic region is governed by a cohesive fracture model, based on two different plastic surfaces: the first surface describes the response in tension and shear and follows a Coulomb slip criterion and the second concerns compressive stress states and accounts for crushing in compression, as shown in Figure 2(b). The material parameters associated with both surfaces degrade based on the

DOI: 10.1002/nme

evolution of the plastic work, hence the post-peak stress-strain behaviour is governed by the fracture energy parameters, defined individually for each failure mode, as can be seen in Figure 2(c). For a detailed description see [15].

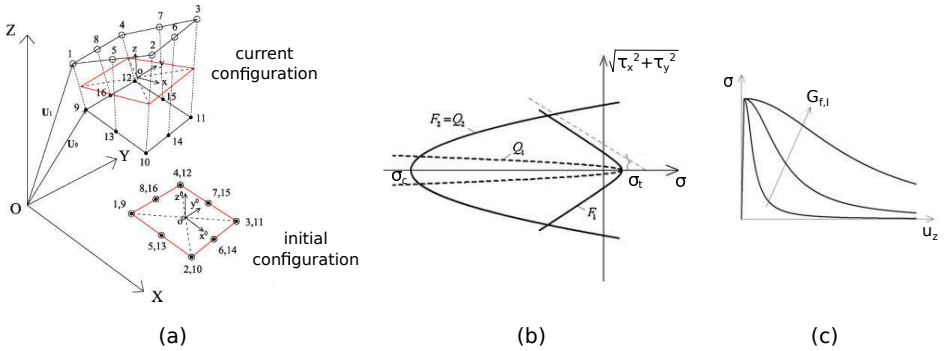

Figure 2. (a) Interface element kinematics, (b) initial plastic surfaces and potentials if interface material model and (c) traction-separation curves in tension [17].

The mesoscale description has allowed the accurate nonlinear analysis of 3D URM structures with arbitrary regular bonding patterns and the prediction of their response up to collapse [14, 15, 17].

2.2. *Domain partitioning*

The use of the mesoscale model is associated with increased computational cost, as highlighted in [17]. To tackle this issue, a domain decomposition technique [16] has been applied in order to divide the large problem into smaller parts, corresponding to subdomains of the structure. The smaller problems are solved in parallel and their solution is assembled to obtain the response of the original domain.

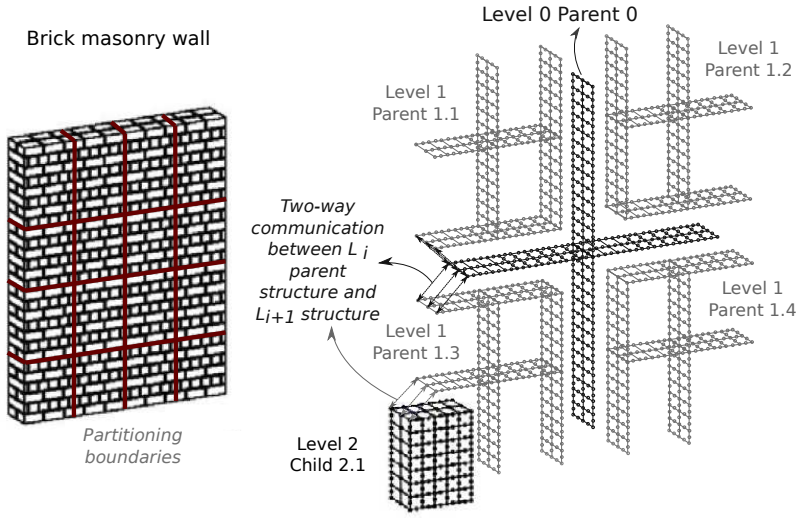

Figure 3. Application of hierarchic domain partitioning to masonry wall.

In the approach employed herein [16], a ”parent structure” composed of dual super-elements is used. Each super-element consists of the boundary nodes of an individual partition and accounts for the two-way communication of the subdomain with the parent structure, which allows the

DOI: 10.1002/nme

parallelisation of the analysis. In this way, the assessment of the nonlinear behaviour is done at the small subdomain scale, while at the structural scale only the assembly of boundary nodes is analysed, leading to increased computational efficiency.

Further improvement can be achieved when using hierarchic partitioning [19], i.e. by further dividing the subdomains with the use of higher level super-elements. In Figure 3, an illustrative example of a two-level hierarchic partitioning of a masonry wall is presented. The hierarchic approach allows the partitioned modelling of a complete heterogeneous structure with mesoscale URM parts, as described in Section 3.2.

3. NUMERICAL STRATEGY FOR COUPLED MASONRY STRUCTURES

3.1. Mesh tying method

In view of the rising complexity of modelling approaches for individual materials, the task of tying meshes with non-matching interfaces is a problem with large practical interest. More specifically, it is necessary when different structural components modelled independently with non-conforming meshes are in contact, as in the case of heterogeneous structures mentioned above, or in cases where sub-domains of the monolithic structure modelled with different level of detail need to be joined together - for example in multi-scale approaches where the critical parts are modelled in a finer scale [20].

The most traditional and commonly used approach for tying dissimilar meshes is the 2D node-to-segment or 3D node-to-surface method (NTS) in which the constraint is imposed on selected points of the interface, called collocation points. Despite its simplicity the nodal collocation approach suffers from certain well-known drawbacks, including the dependency of the results on the choice of master/slave surface, the non-minimisation of gaps and overlaps when the contact conditions are locally satisfied and the inability to pass the standard patch test [21, 22, 23]. In [24] a nodal collocation method with a three-field formulation has been proposed, where an interface frame with an independent displacement field and two Lagrange multiplier (LM) fields is introduced between the coupled meshes. The method passes the first order patch test when the interface frame nodes are chosen based on a proposed criterion, however the extension of this condition in 3D is not readily conceived.

Three-field formulations have also been implemented with interpolated LM fields over the interface frame, achieving large improvement in relative accuracy and efficiency compared to the nodal collocation approaches [22, 23]. When the LM fields are defined as piecewise polynomial on every segment of the interface frame, we obtain the equivalent of a mortar method between the frame and each mesh with the advantage of a potential smoothing of the interface offered by the frame [25]. However, these formulations increase the number of unknowns and the computational cost, thus they are not optimal for modelling large structural systems. Another group of mesh tying methods, such as the first method proposed by Dohrmann et al. in [26], is based on the modification of the elements that face the coupling interface. These methods have been developed for specific cases and cannot be generalised to arbitrary meshes.

The two-field mortar method originally introduced in [27] has been successfully tested in mesh tying and contact problems between dissimilar FE meshes [28, 25, 29], while implementations based on this formulation are available in certain commercial software [30]. Some of its most appealing properties include the fact that it passes the patch test by construction for planar surfaces, it conserves the optimal convergence rate for any type of interface and it explicitly introduces tractions along the interface. Moreover, the admissible shape functions for the LM field which satisfy the LBB conditions and ensure stability are well established in the literature [29].

Alternatives to LM-based formulations for mesh tying have also been investigated. One example is the Nitche method [31], which is a "primal" formulation based only on the displacement variable fields, but is efficient mostly in the elastic case. In [32] the standard finite elements on the interface are enriched using shape functions constructed with the moving least square method and transition

DOI: 10.1002/nme

elements are generated along the interface. The method does not introduce additional unknowns, but is nonetheless computationally expensive and requires the storage of a large amount of information.

Based on the above, a two-field formulation - in two alternative variants - and the principle of a mortar method constraint discretisation have been adopted in this work. In the problem examined herein - i.e. coupled structures with masonry components modelled with a mesoscale approach - an additional consideration arises by the fact that the mesoscale mesh contains cohesive interface elements. Hence the corresponding side of the non-matching interface is not continuous since the element faces do not share nodes along their boundaries. Given this consideration, the implementation of the mesh tying formulation is done in the form of a coupling finite element that consists of two arbitrary faces of solid elements, each one belonging to opposite sides of the tied interface. The implementation of the mesh tying technique in an element-based way is founded on the idea that the coupling terms of the entire interface can be decomposed in the sum of the contributions of each pair of intersecting faces. This implies that the required integration of the fields along the non-matching interface is achieved in a segmented way, pair by pair. The basic characteristics of the formulation and implementation of the coupling element are described below.

3.1.1. Constraint enforcement. The main requirement of a mesh tying formulation is to join two generally non-conforming meshes allowing the consistent transmission of stress and strain fields. For the general setting of the mesh tying problem, we consider two deformable bodies $\Omega^{(i)} \in \mathbf{R}^3, i = 1, 2$ with boundaries $\Gamma^{(i)}$ which can be decomposed into three distinct parts:

$$\partial\Omega^{(i)} = \Gamma_u^{(i)} \cup \Gamma_\sigma^{(i)} \cup \Gamma_c^{(i)} \tag{1}$$

with $\Gamma_u^{(i)} \cap \Gamma_\sigma^{(i)} = \Gamma_u^{(i)} \cap \Gamma_c^{(i)} = \Gamma_c^{(i)} \cap \Gamma_\sigma^{(i)} = 0$. The parts $\Gamma_u^{(i)}$, $\Gamma_\sigma^{(i)}$ and $\Gamma_c^{(i)}$ denote respectively the regions of the boundary where displacements, tractions and mesh tying constraints are imposed. The contacting boundaries of the continuous bodies in the initial configuration are considered coincident $\Gamma_{c,0}^{(1)} = \Gamma_{c,0}^{(2)}$.

Let the displacement field of each body be $\mathbf{u}^{(i)} \in \mathcal{U}^{(i)},\ i = 1, 2$ and $\mathbf{u} = \{\mathbf{u}^{(1)}, \mathbf{u}^{(2)}\}$. The solution space $\mathcal{U}^{(i)}$ for each body is defined as $\mathcal{U}^{(i)} = \{\mathbf{u}^{(i)} \in H^1(\Omega^{(i)}) \mid \mathbf{u}^{(i)} = \bar{\mathbf{u}}^{(i)} \text{ on } \Gamma_u^{(i)}\}$, where $\bar{\mathbf{u}}^{(i)}$ are the imposed displacements along $\Gamma_u^{(i)}$. It is noted that the mesh tying formulation described below is directly applicable considering both small and large deformations. Here, where necessary we will refer to a large displacement framework, as the mesoscale masonry model also accounts for large displacements.

If the sum of the virtual work produced by the internal and the external forces in body $\Omega^{(i)}$ is denoted by $G_{int,ext}^{(i)}$, then from the principle of virtual work we obtain:

$$G_{int,ext}^{(i)}(\mathbf{u}^{(i)}, \delta\mathbf{u}^{(i)}) = \int_{\Gamma_c^{(i)}} \mathbf{t}_c^{(i)} \cdot \delta\mathbf{u}^{(i)}\, dA_0 \quad ,\forall\, \delta\mathbf{u}^{(i)} \in \mathcal{V}^{(i)} \tag{2}$$

where $\mathcal{V}^{(i)} = \{\mathbf{u}^{(i)} \in H^1(\Omega^{(i)}) \mid \mathbf{u}^{(i)} = \mathbf{0} \text{ on } \Gamma_u\}$ is the space of admissible variations of the displacement field $\mathbf{u}^{(i)}$ and $\mathbf{t}_c^{(i)}$ are the tractions over $\Gamma_c^{(i)}$.

Assuming that initially the boundaries are coincident, the tied contact constraint between the continuous bodies $\Omega^{(i)}, i = 1, 2$ at time t formulated in the initial configuration imposes that:

$$\mathbf{g}(\mathbf{u}) = \mathbf{u}^{(1)}(\mathbf{X}^{(1)}, t) - \bar{\mathbf{u}}^{(2)}(\bar{\mathbf{X}}^{(2)}(\mathbf{X}^{(1)}), t) = 0, \quad \text{on } \Gamma_c \tag{3}$$

In equation (3) $\bar{\mathbf{X}}^{(2)}$ signifies the material points on $\Gamma_c^{(2)}$ which correspond to the material points $\mathbf{X}^{(1)}$ of $\Gamma_c^{(1)}$ in the initial configuration, while $\bar{\mathbf{u}}^{(2)}$ are the corresponding displacements.

Constraint (3) is introduced in the weak form of the global boundary value problem by constructing a two field Lagrangian functional representing the contribution of the tied interface in the potential energy of the system:

$$\mathbf{\Pi}_{LM} = \int_{\Gamma_c} \boldsymbol{\lambda} \cdot \mathbf{g}(\mathbf{u})\, d\Gamma \tag{4}$$

DOI: 10.1002/nme

where $\boldsymbol{\lambda} : \Gamma_c \rightarrow \mathbf{R}^3$ is an independent variable field of Lagrange multipliers introduced over the contact interface Γ_c. The Lagrange multiplier field has a direct physical interpretation as it represents the vector of tractions along the contact interface.

Let $\mathcal{M}$ be the vector-valued space of admissible variations of the multiplier field. The variation of the Lagrangian functional in Equation (4) with respect to the Lagrange multiplier field $\boldsymbol{\lambda}$ yields the constraint enforcement equation:

$$\int_{\Gamma_c} \delta\boldsymbol{\lambda} \cdot \mathbf{g}(\mathbf{u}) \, d\Gamma = 0 \qquad , \forall \delta\boldsymbol{\lambda} \in \mathcal{M} \tag{5}$$

while its variation with respect to the displacement field $\mathbf{u}$ yields the tied contact contribution to the virtual work:

$$W_c = \int_{\Gamma_c} \boldsymbol{\lambda} \cdot \frac{\delta \mathbf{g}(\mathbf{u})}{\delta \mathbf{u}} \cdot \delta\mathbf{u} \, d\Gamma \tag{6}$$

where $\delta\mathbf{u} = \{\delta\mathbf{u}^{(1)}, \delta\mathbf{u}^{(2)}\}$ and $\delta\mathbf{u}^{(i)} \in \mathcal{V}^{(i)}$, $i = 1, 2$. The constraint enforcement method based on equations (5) and (6) will be referred to as simple Lagrange Multiplier formulation (LM). The LM formulation results in the exact satisfaction of the tying constraint.

By adding a penalty regularisation to the LM formulation we obtain the Augmented Lagrange Multiplier formulation (ALM):

$$\boldsymbol{\Pi}_{ALM} = \int_{\Gamma_c} [\boldsymbol{\lambda} \cdot \mathbf{g}(\mathbf{u}) + \frac{1}{2}\epsilon \cdot \mathbf{g}(\mathbf{u}) \cdot \mathbf{g}(\mathbf{u})] \, d\Gamma \tag{7}$$

where $\epsilon > 0$ is the penalty parameter. The resulting constraint enforcement equation, stemming from the variation of the ALM functional in Equation (7) with respect to $\boldsymbol{\lambda}$, is identical to Equation (5). On the contrary, the contact contribution to the virtual work, resulting from the variation of the ALM functional with respect to the displacement field $\mathbf{u}$, can be written as follows:

$$W_c = \int_{\Gamma_c} [\boldsymbol{\lambda} \cdot \frac{\delta \mathbf{g}(\mathbf{u})}{\delta \mathbf{u}} \cdot \delta\mathbf{u} + \epsilon \cdot \mathbf{g}(\mathbf{u}) \cdot \frac{\delta \mathbf{g}(\mathbf{u})}{\delta \mathbf{u}} \cdot \delta\mathbf{u}] \, d\Gamma \tag{8}$$

The penalty term vanishes when the constraint is satisfied, which means that it is zero for the solution of the LM formulation. Therefore the two methods provide equivalent results, when the mesh tying constraint is satisfied over the whole contact surface. However, the ALM formulation provides some numerical advantages which will be discussed in the following section.

3.1.2. Interface coupling finite element. **Discretisations for 2nd order meshes:** The coupling finite element proposed here is implemented for both the LM and the ALM formulations described in the previous section. The two adjacent bodies are discretised with second order 3D FE meshes. More specifically, the discretised coupled domains $\Omega_h^{(i)}$, $i = 1, 2$, are meshed either with 20-noded hexahedra, 15-noded wedges or 10-noded tetrahedra. In the discrete form, the two sides of the non-conforming interface, $\Gamma_c^{(1),h}$ and $\Gamma_c^{(2),h}$ are not necessarily coincident, therefore a distinction must always be made between them.

The coupling element consists of two intersecting segments of the non-conforming contact interface, as shown in Figure 4. Each segment i ($i = 1, 2$) is the face of a solid element of domain $\Omega_h^{(i)}$ belonging to one side of the non-conforming interface $\Gamma_c^{(i),h}$. Based on the type of meshes considered for the coupled domains, each segment i is either a 6-noded triangle or an 8-noded quadrilateral. Let n_i be the number of nodes of segment i ($n_i = 6$ or 8). The nodal displacement vectors $\mathbf{u}_k^{(i)} \in \mathbf{R}^3$, $k = 1, n_i$ are interpolated within segment i based on the projection on the interface $\Gamma_c^{(i),h}$ of the displacement field of the corresponding bulk mesh $\Omega_h^{(i)}$. The approximation of the interface displacement field within a segment i can be written as:

$$\mathbf{u}_h^{(i)}(\mathbf{X}, t) = \sum_{k=1}^{n_i} N_k^{(i)}(\mathbf{X}^{(i)}) \, \mathbf{u}_k^{(i)}(t) \tag{9}$$

DOI: 10.1002/nme

$N_k^{(i)}$ are quadratic shape functions in the case of triangular 6-noded segments and serendipity shape functions in the case of quadrilateral 8-noded segments.

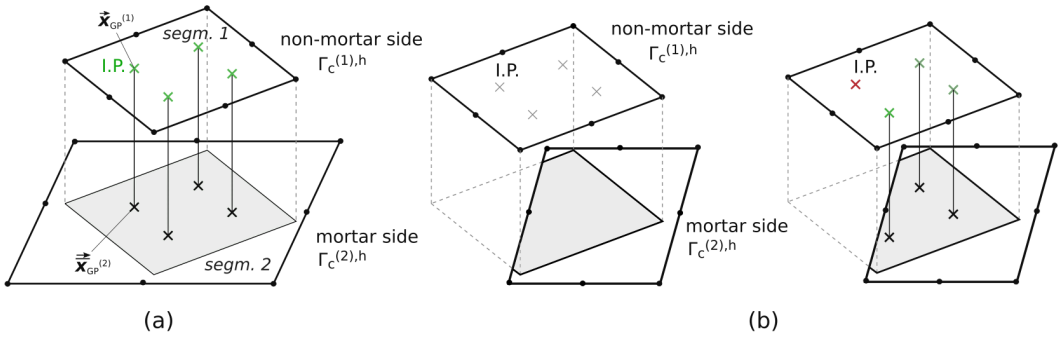

Figure 4. Interface coupling element with $n_1 = 8$ and $n_2 = 8$.

The Lagrange multipliers are defined as piecewise polynomial fields on one of the two sides of the interface, which is called the *non-mortar* side and will be denoted as $\Gamma_c^{(1),h}$. The opposite side $\Gamma_c^{(2),h}$ is called *mortar* side. The choice of the non-mortar side is common for all the coupling elements along a given contact interface.

Two alternatives have been implemented regarding the Lagrange multiplier shape functions $\Phi_k(\mathbf{X}^{(i)})$. In the first case, additional Lagrange multiplier parameters are defined on all the nodes of the non-mortar segment and they are interpolated with second order shape functions: $\Phi_k(\mathbf{X}^{(i)}) = N_k(\mathbf{X}^{(i)})$ for $k = 1 : n_1$. In the second case only the corner nodes of the non-mortar side segment hold Lagrange multipliers and the shape functions $\Phi_k(\mathbf{X}^{(i)})$ for $k = 1 : n_1/2$ are linear.

$$\boldsymbol{\lambda}_h(\mathbf{X}^{(1)}, t) = \sum_{k=1}^{n_\lambda} \Phi_k(\mathbf{X}^{(i)})\, \boldsymbol{\lambda}_k(t) \tag{10}$$

where n_λ is the number of non-mortar side nodes that hold Lagrange multiplier unknowns.

Consistent stiffness matrix and internal force vector: Let the vector of the coupling element degrees of freedom (DOFs) be noted as: $\mathbf{u}^{(e)} = [\mathbf{u}^{(1)}, \mathbf{u}^{(2)}, \boldsymbol{\lambda}^{(1)}]^T$, where $\mathbf{u}^{(i)}$, $i = 1, 2$, is the vector of the nodal DOFs of segment i with size $3n_i$ and $\boldsymbol{\lambda}^{(1)}$ is the vector of the Lagrange multiplier unknowns of segment 1 with size $3n_\lambda$. The LM formulation of equations (5) and (6), with the above discretisations results in the following stiffness matrix for the coupling element:

$$\mathbf{K}_h^{(e)} = \begin{bmatrix} \mathbf{0} & \mathbf{0} & \mathbf{C_1} \\ \mathbf{0} & \mathbf{0} & -\mathbf{C_2} \\ \mathbf{C_1}^T & -\mathbf{C_2}^T & \mathbf{0} \end{bmatrix} \tag{11}$$

where:

$$\mathbf{C}_1 = \sum_{k=1}^{n_\lambda} \sum_{l=1}^{n_1} \int_{\Gamma_{c,h}^{(1)}} \mathbf{\Phi}_k(\mathbf{X^{(1)}}) \mathbf{N}_l^{(1)}(\mathbf{X}^{(1)}) d\Gamma_{c,h} \tag{12}$$

$$\mathbf{C}_2 = \sum_{k=1}^{n_\lambda} \sum_{l=1}^{n_2} \int_{\Gamma_{c,h}^{(1)}} \mathbf{\Phi}_k(\mathbf{X^{(1)}}) \mathbf{N}_l^{(2)}(\mathbf{X}^{(2)}) d\Gamma_{c,h} \tag{13}$$

The zero diagonal terms in $\mathbf{K}_h^{(e)}$ could result in numerical problems in the solution of the final system of equations, when certain classes of solution methods are employed. More specifically, in the context of a solution procedure such as the Frontal method [33] in which constraint equations are

DOI: 10.1002/nme

used to eliminate the Lagrange multipliers and row switching is not included, the nodal parameters need to be eliminated before the Lagrange multipliers. In certain cases the zero diagonal terms in $\mathbf{K}_h^{(e)}$ associated with nodal degrees of freedom renders this impossible. For example, in the model shown in Figure 5, after the assembly of the unrestrained element 1 and the coupling element, the nodal DOFs cannot be eliminated since the resulting submatrix is singular.

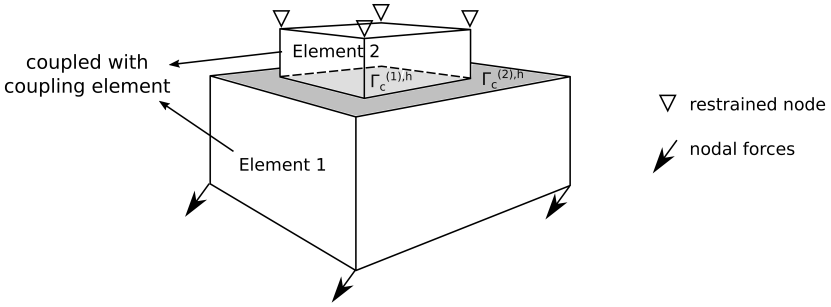

Figure 5. Investigation of the robustness of the LM formulation with the Frontal method.

One remedy to this problem is the use of the ALM formulation as given in Equations (5) and (8), which results in an element stiffness matrix with the following structure:

$$\mathbf{K}_h^{(e)} = \begin{bmatrix} \mathbf{P_{11}} & -\mathbf{P_{12}} & \mathbf{C_1} \\ -\mathbf{P_{21}} & \mathbf{P_{22}} & -\mathbf{C_2} \\ \mathbf{C_1}^T & -\mathbf{C_2}^T & \mathbf{0} \end{bmatrix} \tag{14}$$

where:

$$\mathbf{P}_{11} = \sum_{k=1}^{n_1}\sum_{l=1}^{n_1} \int_{\Gamma_{c,h}^{(1)}} \epsilon\, \mathbf{N}_k^{(1)}(\mathbf{X}^{(1)})\mathbf{N}_l^{(1)}(\mathbf{X}^{(1)}) d\Gamma_{c,h} \tag{15}$$

$$\mathbf{P}_{22} = \sum_{k=1}^{n_2}\sum_{l=1}^{n_2} \int_{\Gamma_{c,h}^{(1)}} \epsilon\, \mathbf{N}_k^{(2)}(\mathbf{X}^{(2)})\mathbf{N}_l^{(2)}(\mathbf{X}^{(2)}) d\Gamma_{c,h} \tag{16}$$

$$\mathbf{P}_{12} = \mathbf{P}_{21}^T = \sum_{k=1}^{n_1}\sum_{l=1}^{n_2} \int_{\Gamma_{c,h}^{(1)}} \epsilon\, \mathbf{N}_k^{(1)}(\mathbf{X}^{(1)})\mathbf{N}_l^{(2)}(\mathbf{X}^{(2)}) d\Gamma_{c,h} \tag{17}$$

The zero diagonal terms have vanished and the solution of the problem is theoretically equivalent to the one obtained by the LM formulation for $\epsilon > 0$, see Section 3.1.1. In practise, the penalty parameter ϵ must be within certain limits to avoid ill-conditioning [34]. The stiffness matrices in (11) and (14) depend only on the initial configuration and therefore can be calculated just once at the beginning of the analysis. The internal force vector at each step is calculated by:

$$\mathbf{F}_{int}^{(e)} = \mathbf{K}_h^{(e)} \cdot \mathbf{u}^{(e)} \tag{18}$$

Integration scheme: The calculation of the coupling terms $\mathbf{C}_1$, $\mathbf{P}_{11}$ and $\mathbf{P}_{22}$ is straightforward, as they refer to integration of non-mortar side fields on the non-mortar side itself. On the contrary, the calculation of $\mathbf{C}_2$ and $\mathbf{P}_{12}$ involves the integration of quantities defined both on $\Gamma_c^{(1),h}$ and on $\Gamma_c^{(2),h}$ over the non-mortar side $\Gamma_c^{(1),h}$. As the two sides are non-conforming, the polynomial functions inside the integrals are generally not continuous along the entire segment $\Gamma_c^{(1),h}$. One way to deal with this issue is to divide the non-mortar segment $\Gamma_c^{(1),h}$ into subdomains with smooth

DOI: 10.1002/nme

interpolations of the fields on both sides. However, the computational cost of this procedure is large. Hence, an approximate integration scheme has been used to increase the efficiency of the algorithm. More specifically, Guassian quadrature with integration points (IPs) defined along the entire non-mortar segment is used. The IPs are projected on the mortar side, as shown in Figure 4, and the calculation of the integral relies on the calculation of the functions at each IP on $\Gamma_c^{(1),h}$ and at each IP-projection point on $\Gamma_c^{(2),h}$. For an indicative function $M(\boldsymbol{\xi}^{(1)}, \boldsymbol{\xi}^{(2)})$ this scheme would lead to:

$$\int_{\Gamma_{c,h}^{(1)}} M(\boldsymbol{\xi}^{(1)}, \boldsymbol{\xi}^{(2)}) d\Gamma_{c,h} = \sum_{ip=1}^{n_{ip}} M(\boldsymbol{\xi}_{ip}^{(1)}, \bar{\boldsymbol{\xi}}_{ip}^{(2)})\ J_{seg^{(1)}}\ w_{ip} \tag{19}$$

where n_{ip} is the number of IP on a non-mortar segment, w_{ip} is the weight corresponding to each point, $\boldsymbol{\xi}^{(i)} = (\xi_1^{(i)}\ \xi_2^{(i)})$, $i = 1, 2$ the parametric spaces of segments $\Gamma_c^{(1),h}$ and $\Gamma_c^{(2),h}$ respectively and $J_{seg^{(1)}} = \| \frac{\partial \mathbf{x}^{(1)}}{\partial \xi_1^{(1)}} \times \frac{\partial \mathbf{x}^{(1)}}{\partial \xi_2^{(1)}} \|$ is the jacobian of the mapping from the physical space to the non-mortar segment parameter space. If the projection of an IP is located outside of the mortar segment, then it is considered inactive, i.e. $w_{ip} = 0$.

This scheme gives an accurate calculation of the integrals when the projection of the non-mortar segment is entirely inside the mortar segment, as in Figure 4 (a), or when the two sides are matching. However, it introduces an error in the general case of arbitrarily intersecting segments, as in the case depicted in Figure 4 (b). Nevertheless, when the non-mortar side has a finer discretisation than the mortar side - as is the usual practise - and the number of IPs is large, then this error tends to zero and the integration method is sufficiently accurate as shown in Section 3.1.3.

It is finally noted that a closest point projection algorithm has been developed for the projection of the IPs from $\Gamma_c^{(1),h}$ to $\Gamma_c^{(2),h}$. The algorithm is based on the normal field of the non-mortar side, thus avoiding multiple projections.

3.1.3. Numerical verification of interface coupling element. Initially, we validate the performance of the mesh tying element through a patch test which examines the ability of the coupling scheme to transmit a constant stress field between two elastic domains. As mentioned above, the mortar method passes the patch test by construction when the interfaces are planar. The test shown in Figure 6 (a) examines the case of a planar but inclined interface. The block is restrained from rigid body motions and a uniform stress field of -1 is applied in the vertical direction (z). The resulting σ_{zz} field is plotted. The patch test is not exactly satisfied in the non-conforming case, due to the choice of an approximate integration scheme as explained in the previous section. However, this error is small for the analysis purposes examined here and is significantly reduced when increasing the number of IPs, as shown in Figure 7.

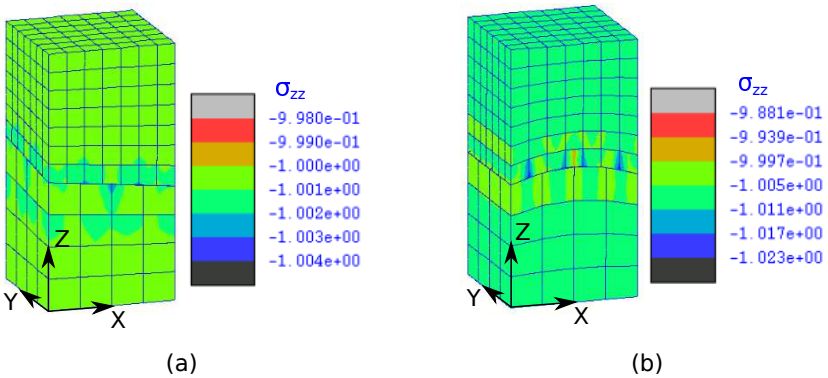

Figure 6. Patch test results: σ_{zz} field for LM formulation with quadratic multipliers for (a) planar inclined interface and (b) curved interface.

DOI: 10.1002/nme

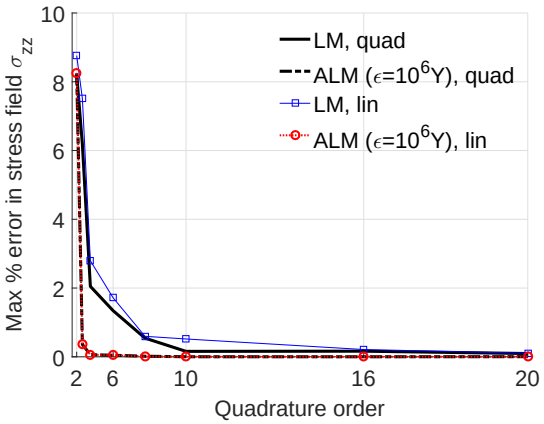

Figure 7. Patch test results: maximum error in the σ_{zz} field with respect to the number of integration points of the coupling element.

A parametric study with respect to the penalty parameter ϵ has shown that the ALM formulation provides equivalent results to the LM formulation in the patch test when $\epsilon \leq Y \cdot 10^3$ and progressively improved accuracy as the values of the penalty parameter increases from $Y \cdot 10^3$ to $Y \cdot 10^6$, where Y is the Young's modulus of the contacting bodies. However, the error rapidly rises when the penalty parameter increases further, due to ill-conditioning of the problem. When the coupled bodies have different Young's moduli, the penalty parameter should be estimated based on the lower value. The results in Figure 7 correspond to $\epsilon = Y \cdot 10^6$. When the coupling interface contains gaps or overlaps, the mortar method is not expected to accurately pass the patch test [23], but it usually achieves a much better performance than the NTS approaches. Figure 6 (b) shows the patch test results in the case of a curved interface for the LM formulation with quadratic LM field and 10×10 IPs. In this case, when the number of IPs increases the error converges to a non-zero value of approximately 2.5%. It is noted that the patch test is passed to machine accuracy for both planar and curved interfaces in the case of matching meshes, as expected theoretically.

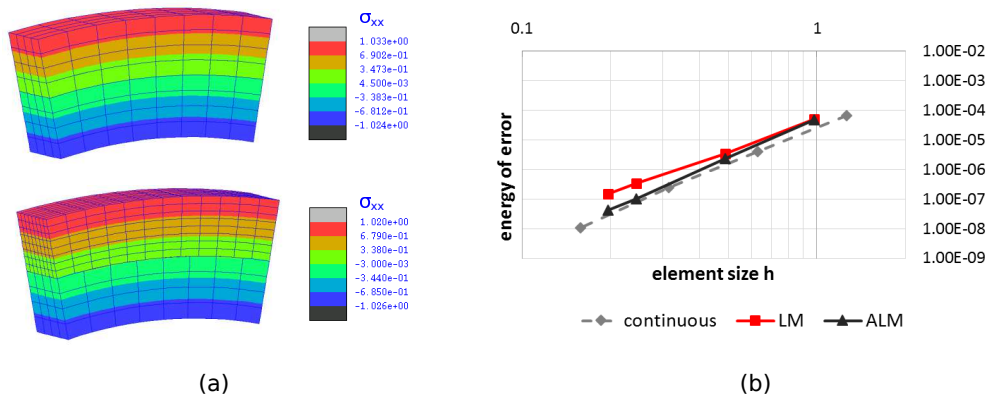

Figure 8. Convergence of the discretisation error measured in the energy norm with uniform mesh refinement of a bending beam structure.

The second validation test examines the convergence rate with mesh refinement. A beam in pure bending conditions is modelled, first with a continuous mesh and then with two independently meshed layers combined with the mesh tying elements, see Figure 8 (a). As shown in Figure 8 (b) the convergence rate in the energy norm is conserved for the LM scheme, while it is slightly increased when using the ALM scheme with second order LM field.

DOI: 10.1002/nme

3.2. *Coupled masonry structures with non-matching interfaces*

The mesh tying method described above allows the tied coupling of dissimilar interfaces between 3D meshes and therefore it can be used for the connection of parts of heterogeneous structures which are meshed independently. In general, each one of these parts - or structural components - is partitioned in order to increase the computational efficiency of the model. In this case the mortar tying method is used to couple the non-conforming parent structures of the partitioned components on the level 0 structure, as shown in Figure 9.

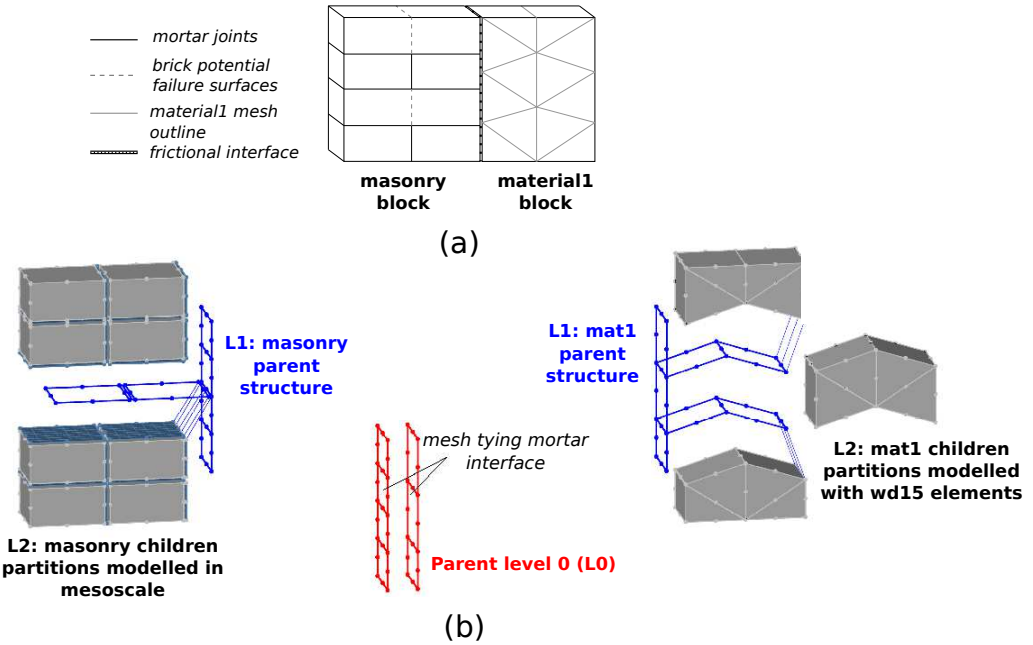

Figure 9. Example of the modelling strategy for heterogeneous structures - masonry block coupled with continuous mesh of 15-noded wedge elements: (a) front view and (b) outline of partitioned model with 2-level hierarchical partitioning.

In order to model the coupling of masonry components with other material meshes in a realistic way, the physical behaviour of the coupling interface must also be considered. For this purpose a layer of nonlinear cohesive interface elements is attached to the masonry side of the non-conforming interface to account for the interaction. The same type of interface element and constitutive law described in Section 2.1 is used, with adjusted material properties to capture the interaction between structural components that can include decohesion in tension and strength softening and frictional sliding in shear. These interface elements can belong either to the level 0 parent structure or to the highest level children partitions, as part of the mesoscale masonry model. The latter choice has been adopted in the applications presented below, as the computational cost corresponding to the nonlinear interface elements is divided and transferred to the parallel processes.

4. NUMERICAL EXAMPLES

The partitioned masonry model and the non-conforming interface coupling scheme have been implemented into the nonlinear structural analysis program ADAPTIC [35]. This section presents the results obtained by numerical models of heterogeneous masonry structures built based on the approach described in the previous sections. These include two types of single-span arch bridge with infill soil material and one multi-leaf wall loaded out-of-plane. Numerical predictions are compared

DOI: 10.1002/nme

to numerical and experimental results found in the literature to show the potential of the strategy proposed here for the detailed 3D modelling and the reliable analysis of complex coupled masonry structures.

4.1. Arch bridge

The first set of numerical examples presented here is based on the modelling of two single-span arch bridge specimens with spandrel walls and soil backfill material which were tested experimentally by Melbourne et al. [36].

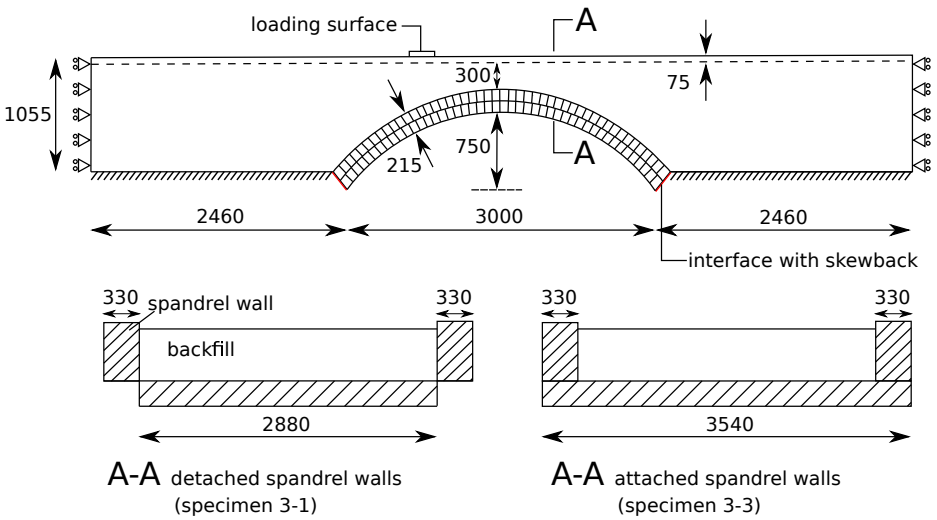

Figure 10. Front view and cross sections of modelled part of bridge specimens 3-1 and 3-3 (dimensions in mm).

Initially, bridge models with matching element faces between the arch and the backfill connected with zero-thickness interface elements have been developed. These models are referred to as ”conforming”. Subsequently, the more efficient modelling approach described in Section 3 is applied for the simulation of the same structure. In this case the masonry arch and the backfill domain are modelled independently without mesh compatibility considerations and are connected through a non-matching interface tied with the mortar method; hence, the respective models will be referred to as ”non-conforming”. The results of the two types of models are contrasted to investigate: i) the benefits in terms of computational efficiency when the backfill material is modelled independently with a coarser mesh and ii) the level of accuracy attained when using the non-matching mesh tying method. Furthermore the numerical results are compared with the experimental outcomes to show the potential of the proposed strategy in predicting the actual behaviour of coupled masonry structures.

Two of the specimens of the experimental set-up in [36] have been investigated: specimen 3-1, in which the spandrel walls are detached from the arch and only provide confinement to the backfill material and specimen 3-3 in which the spandrel walls are attached to the arch. The geometric characteristics of the modelled part of the bridge specimens are shown in Figure 10. The skewbacks supporting the arches have been replaced by restraints as their deformation has been considered negligible. Additionally, the part of the spandrel walls and the backfill below the level of the arch has not been modelled, as it was not considered critical. The arch consists of two rings, each one containing 48 bricks along the direction of the circumference and 10 along the width of the bridge. The springing angle of the arch is 37°. The main mechanical properties of the masonry and the backfill material are given in Tables I and II. A distributed loading is applied on the top of the backfill along an area of $200 \times 2200 mm^2$ at the level of quarter-span.

DOI: 10.1002/nme

Table I. Mechanical properties of backfill material.

Elastic modulus $E_f(N/mm^2)$	Poisson's ratio ν_f	Cohesion $c_f(N/mm^2))$	Friction angle ϕ_f	Unit weight $\rho_f(kN/m^3)$
200	0.20	0.001	50^o	19.1

Table II. Mechanical properties of masonry of arch bridge.

Bricks	Elastic modulus $E_b(N/mm^2)$	Poisson's ratio ν_b	Unit weight $\rho_b(kN/m^3)$	
	35000	0.15	24.3	
Brick-mortar interface	Normal stiffness $K_n\ (N/mm^3)$	Tangent stiffness $K_t\ (N/mm^3)$	Tensile strength $\sigma_{t0}(N/mm^2)$	Cohesion $c_i(N/mm^2)$
	400	167	0.2	0.29
	Friction angle $\phi_0(degrees)$	Fracture energy $G_{fI}(N/mm)$	Fracture energy $G_{fII}(N/mm)$	
	26	0.02	0.12	

4.1.1. Detached spandrel walls. In the case of detached spandrel walls, practically the main contribution of the walls is the confinement of the backfill along the transverse direction, while the arch is considered to have a uniform behaviour along the width. Based on the above, it is assumed that the response of the bridge can be represented using a strip model with one layer of elements along the thickness and restrained transverse displacements for the backfill to account for the confinement provided by the spandrels.

One *'conforming'* and a series of *'non-conforming'* strip models of specimen 3-1 have been constructed, for comparison purposes. All models are partitioned in two domains: i) the arch which is simulated with the detailed mesoscale description and is identical in all models and ii) the backfill material modelled with varying number of 15-noded wedge elements. Each non-conforming model is characterised by the number of backfill (soil) elements along the coupling interface, (e.g. model '*non-conf-10*' contains 10 soil element faces along the arch-backfill interface).

Table III. Number of DOFs and speed-up for bridge with detached spandrel walls.

Strip model	Nb soil elem.	Soil part.DOFs	Parent struc.DOFs	T_c/T_{nc}
conforming	371	5640	729	-
non-conf-10	109	1773	888	2.645
non-conf-15	134	2148	963	2.414
non-conf-20	173	2727	1038	2.249
non-conf-25	208	3237	1113	2.037
non-conf-30	259	3978	1188	1.845
non-conf-40	309	4728	1338	1.515

Linear elastic analysis. In order to assess the computational benefit and the accuracy of the *'non-conforming'* modelling scheme, elastic analysis has been performed for the different models of specimen 3-1. Table III summarises the computational performance of the different non-conforming strip models with respect to the conforming case, also visualised in Figure 11(a). All the results refer to a 5-step fully elastic analysis using three processors. The *wall-clock time ratio* T_c/T_{nc} is the ratio between the analysis time of the conforming model T_c and the one of the non-conforming model T_{nc}. Significant speed-up is observed for all the non-conforming models.

Furthermore, a first assessment of the accuracy of the mesh tying scheme in transmitting stress and displacement fields can be made by examining the Load - Deflection curves in Figure 11(b), where the deflection refers to the displacement of the bottom of the arch at quarter span. It is evident that the elastic response is practically identical between the conforming and the non-conforming case,

DOI: 10.1002/nme

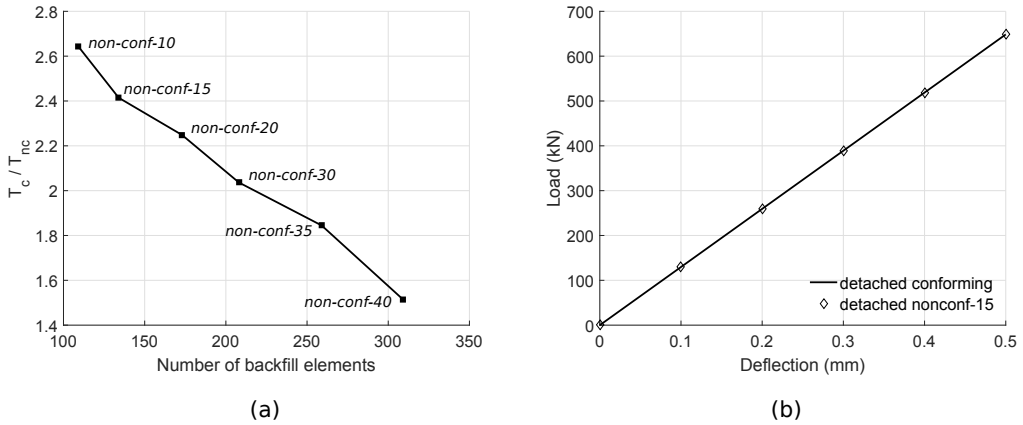

Figure 11. (a) Wall-clock time ratios for elastic analysis of non-conforming models with different backfill meshes. (b) Elastic response of conforming and non-conforming models.

even for a backfill mesh as coarse as that of the $'non-conf-15'$ model, demonstrating that the coupling scheme is sufficiently accurate.

Nonlinear analysis. Subsequently, a nonlinear analysis of the models of specimen 3-1 has been performed, simulating the experimental test of Melbourne et al [36]. A modified Druker-Prager constitutive model [37] with a tensile cap is employed for the simulation of the backfill material. The main material parameters of the nonlinear models are listed in Tables I and II. Figure 12 shows the global response of the conforming and two non-conforming models, in comparison to the experimental results [36]. The wall-clock time of the analysis in each case is also reported.

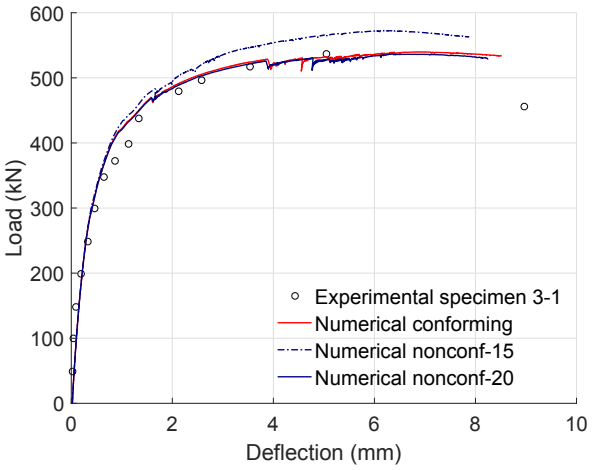

Time of analysis (min)	
conforming	181
nonconf-15	110
nonconf-20	126

Figure 12. Global response of conforming and non-conforming nonlinear models of specimen 3-1: total load applied - arch deflection at quarter-span.

Initially, based on the results of the elastic analysis, the model *'non-conf-15'* has been chosen for the optimal combination of accuracy and speed-up. However, this model has shown a slightly stiffer nonlinear behaviour compared to the conforming one. Therefore, the next level of refinement

DOI: 10.1002/nme

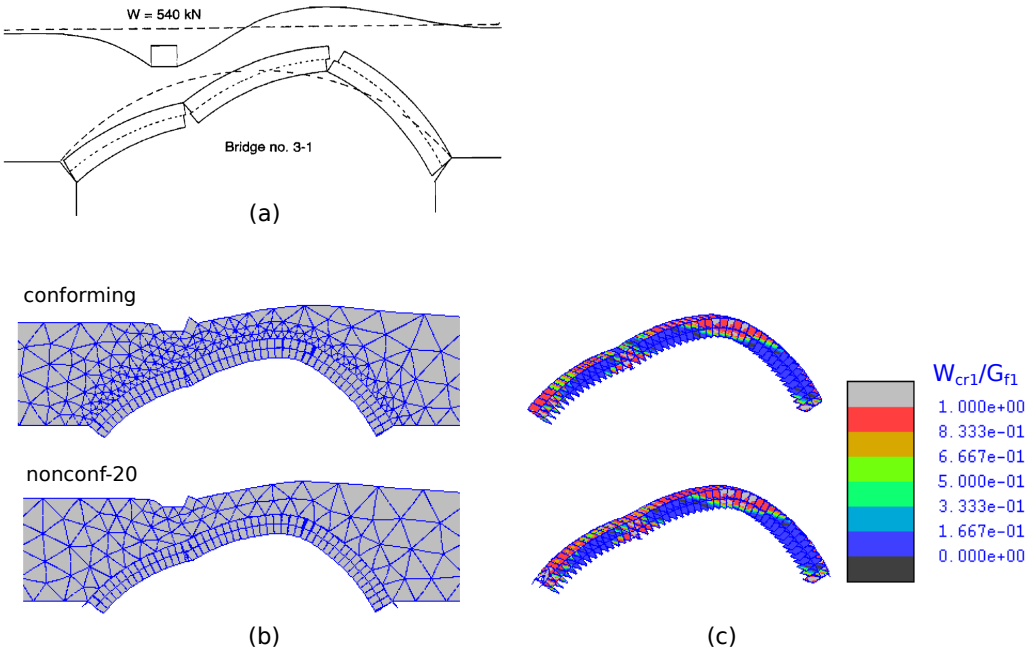

Figure 13. (a) Experimental cracking pattern [36]; (b) Deformed shape of *'conforming'* and *'non-conf-20'* model at collapse; (c) Plastic work developed in the arch interface elements at collapse.

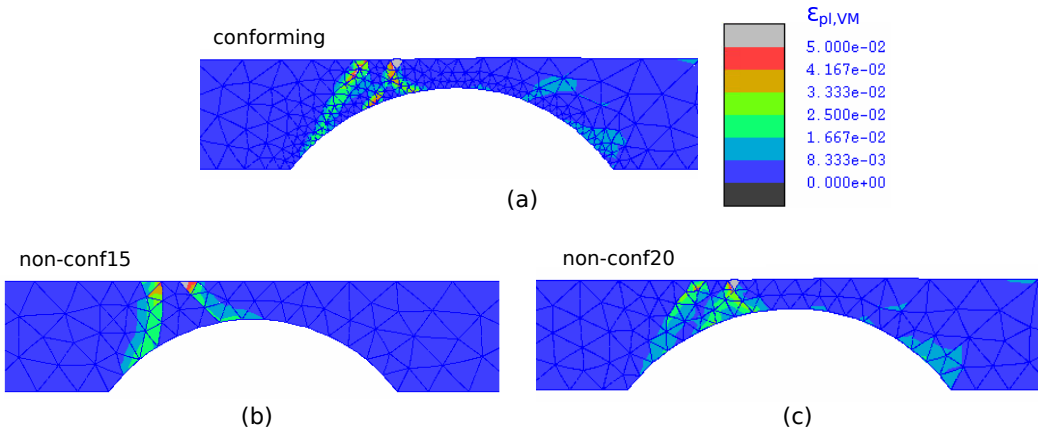

Figure 14. Plastic deformation in the backfill material at the onset of the forth hinge (a) in the conforming model, (b) in the *'non-conf-15'* model and (c) in the *'non-conf-20'* model.

has been considered, i.e. model *'non-conf-20'*. In this case, the non-conforming model results in an almost identical behaviour to the conforming model, while the ratio T_c/Tnc for the non-linear analysis is 1.437. The stiffer response of the *'non-conf-15'* model is probably due to insufficient refinement of the mesh of the backfill domain for the nonlinear case. As illustrated in Figure 14 this coarse mesh does not capture the distribution of the plastic strains with sufficient accuracy.

Comparing the numerical results with the experimental curve, a close agreement can be observed in the initial elastic stiffness, the nonlinear pre-peak behaviour, the peak load and the corresponding deflection. Furthermore, the cracking pattern developed in the numerical models is the same as the

DOI: 10.1002/nme

one observed experimentally, as shown in Figure 13. More specifically, a 4-hinge mechanism is clearly observed with fully damaged interfaces in the area of the hinges at collapse. In parallel, sliding occurs along the interface between the arch and backfill.

4.1.2. Attached spandrel walls. In the case of specimen 3-3 the contribution of the spandrel walls is not limited to the confinement of the backfill. Being attached to the arch they also contribute to the ultimate strength and stiffness of the structure, as shown experimentally [36]. Therefore the assumption on which the strip model of specimen 3-1 is based does not hold and a full 3D model including the spandrel walls needs to be employed to obtain a realistic representation of the structure.

A simplified approach has been employed here. The spandrel walls have been modelled with 15-noded wedge elements, hence a macroscale description of the masonry constitutive behaviour is adopted. The meshes of the lateral walls and backfill material are continuous, meaning that the physical behaviour of the interface between them is ignored.

Exploiting the longitudinal symmetry of the structure, only half of the bridge specimen is represented, considering additional restraints in the transverse direction for all the nodes of the symmetry plane. A conforming model and a series of non-conforming models of specimen 3-3 have been built. In all the cases the mesostructure of the arch is represented in detail. The non-conforming models are characterised by the number of element faces belonging to the backfill/spandrel wall domain that reside on the interface between backfill and arch (e.g. in model '*3Dnon-10x3*' the backfill/spandrel domain contains 10 element faces along the arch circumferential direction and 3 layers of elements along the width).

Linear elastic analysis. As in the case of specimen 3-1, the different models of specimen 3-3 have been tested in elastic analysis to investigate their computational performance and the accuracy of the mesh tying scheme in the elastic region. Figure 15(a) shows that in the case of full 3D modelling the speed-up achieved with the independent meshing of the backfill material compared to the conforming model is significant. In parallel, the elastic response, plotted in Figure 15(b) in terms of total vertical load on top of the backfill and corresponding deflection at the quarter-span of the arch at the symmetry plane, is identical even for a model as coarse as '*3Dnon-22x4*'. It is noted that the response of the specimen 3-3 model is stiffer than the specimen 3-1 model, as can be observed in Figure 15(b), due to the contribution of the lateral walls.

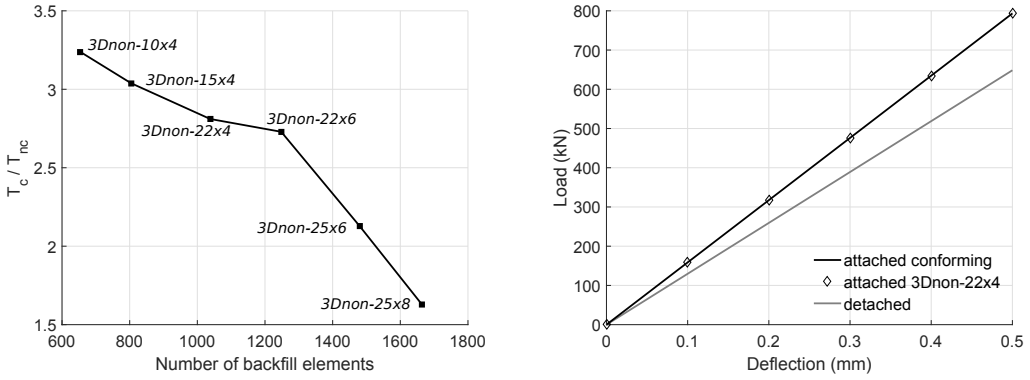

Figure 15. (a) Wall-clock time ratios for elastic analysis of non-conforming models with different backfill meshes. (b) Elastic response of conforming and non-conforming models.

Nonlinear analysis. Subsequently, the *'3Dnon-22x4'* model has been employed for the nonlinear analysis of specimen 3-3 under the experimental loading conditions. A realistic time limit of 144 hours was set for the nonlinear analysis. Within this limit, it is possible to obtain the ultimate

DOI: 10.1002/nme

capacity of the bridge and the numerical prediction of the failure mechanism using the non-conforming model. On the contrary, the computational time required for the nonlinear analysis of the conforming model with attached spandrels is prohibitive, which demonstrates the significant potential of the suggested modelling strategy for the simulation of real scale structures.

The parameters of the nonlinear models corresponding to the arch and the backfill are the same as the ones used for the model of specimen 3-1, reported in Tables I and II. The nonlinear behaviour of the spandrel walls is approximated using the modified Druker-Prager model [37] with the parameters listed in Table IV.

Table IV. Material properties assumed for the spandrel walls.

Elastic modulus $E_w(N/mm^2)$	Poisson's ratio ν_w	Cohesion $c_w(N/mm^2)$	Friction angle ϕ_w	Unit weight $\rho_w(kN/m^3)$
4000	0.2	0.2	30^o	24.3

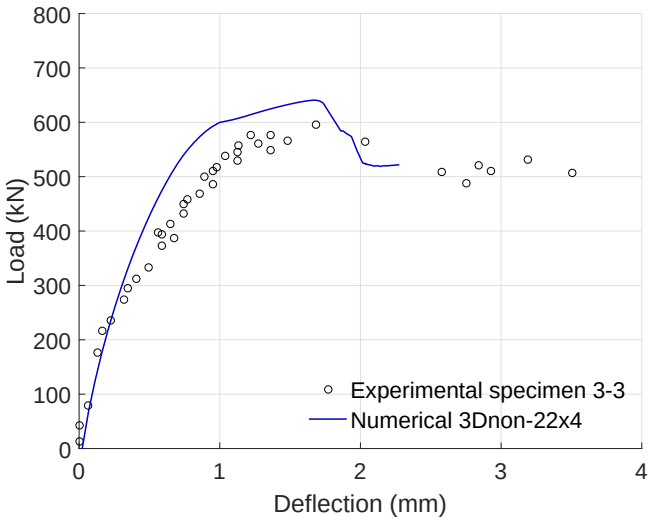

Figure 16. Global response of non-conforming nonlinear model of specimen 3-3: total load applied - arch deflection at quarter span.

Figure 16 shows the global response curve obtained by the non-conforming model *'3Dnon-22x4'* compared to the experimental response of specimen 3-3. The model accurately captures the initial stiffness of the specimen and the increased load capacity of the bridge when the spandrel walls are attached to the arch. Furthermore, the arch deflection at the maximum load predicted by the numerical model and measured in the test are in close agreement. Finally, the numerical result reproduces the post-peak residual strength of the bridge at the level of arch deflection corresponding to the final stage of the analysis.

The experimental cracking pattern of specimen 3-3 [36] is shown in Figure 17(a). The development of plastic deformation in the spandrel wall elements, shown in Figure 18(a), approximately reproduces the effect of the spandrel wall cracking pattern observed experimentally. The backfill material plastic deformation is presented in Figure 18(b). Large plastic deformations are observed below the loading and close to the interface with the spandrel walls. Evidently there is a tendency for separation and sliding along this interface.

Figure 17(b) depicts the deformed shape of the arch domain at the end of the numerical analysis, while Figure 19 shows the plastic work developed in the interface elements of the arch domain as a fraction of the fracture energy for Mode-I. These two figures reveal the formation of a four hinge mechanism in the arch and the development of ring separation around the central hinges.

DOI: 10.1002/nme

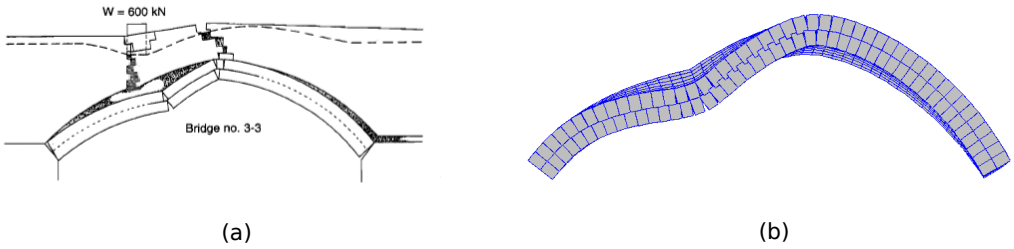

Figure 17. (a) Experimental cracking pattern of specimen 3-3 [36]; (b) Deformed shape of arch at the end of numerical analysis.

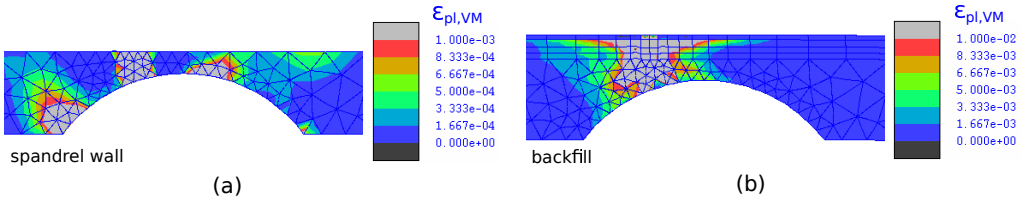

Figure 18. (a) Plastic deformation developed in spandrel walls at peak load; (b) Plastic deformation developed in backfill at peak load.

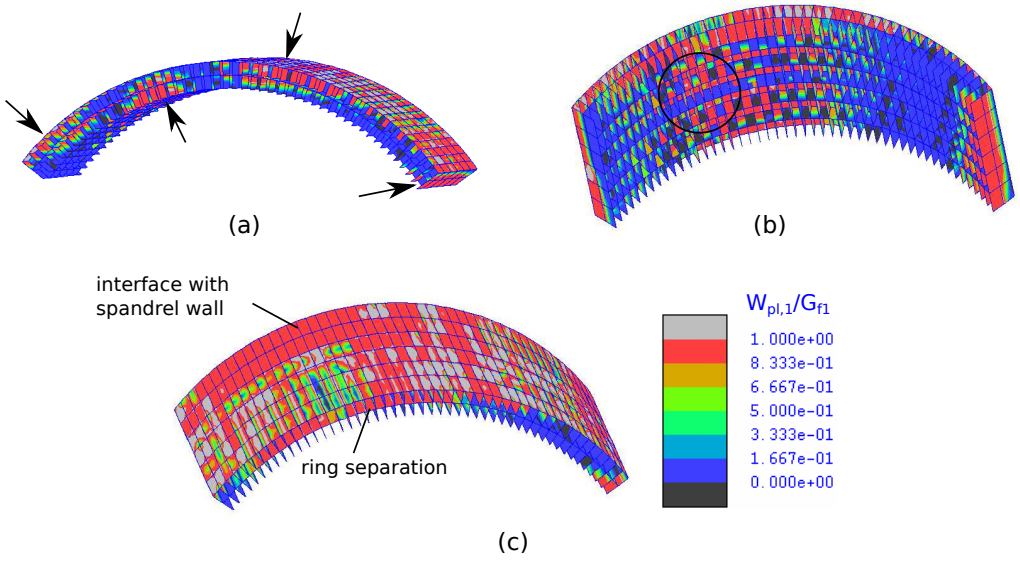

Figure 19. Plastic work developed in IN16 elements of arch and arch-backfill interface: (a) Bottom/side view; (b) Bottom view; (c) Top view.

The position of the hinges is noted in Figure 19(a) while the area where ring separation occurs can be observed in Figure 19(b). This failure mechanism is in very close agreement with the experimental cracking pattern of the arch, shown in Figure 17(a). In addition, Figure 19(b) shows the developments of longitudinal cracks at the bottom of the arch. The influence of the longitudinal

DOI: 10.1002/nme

cracking can only be taken into account with a full 3D modelling of the structure, as the one employed here. Finally, the interface elements between the arch and the backfill develop extensive damage due to sliding, as shown in Figure 19(c). In particular, the interfaces below the spandrel wall are entirely damaged, indicating separation between the wall and the arch, also observed experimentally.

It is worth noting that the coupling method described in Section 3 allows the realistic mesoscale modelling of the spandrel walls and their coupling with both the arch and the backfill material, taking into account the physical interaction between each component. This detailed model would be able to represent all the mechanisms that contribute to the degradation of the structure, including sliding between the backfill material and the spandrel walls. This further refinement of the bridge models is not treated in the present work, as the objective here is to present relatively simple indicative examples that demonstrate the potential of the proposed method, but it will be the subject of further studies.

4.2. Multi-leaf wall

The second numerical example, which demonstrates the potential of the proposed computational strategy for the realistic modelling of coupled masonry structures, is the nonlinear analysis of multi-leaf walls. Typical construction components in historical structures, multi-leaf walls generally consist of two external brick-block masonry panels confining a layer of infill material. The infill material is most commonly made of some type of gravel or cobblestone mixed with mortar or soil.

The accurate simulation of this type of heterogeneous structural components in a simplified/macroscopic way is not straightforward, as the influence of all individual parts and their interaction should be properly taken into account; hence only a few studies have been conducted thus far on the behaviour of multi-leaf walls. One of them is the work of Milani [6] on the limit analysis of multi-leaf walls before and after reinforcement with composite materials. One of the structures studied by Milani is a generic configuration of a brick multi-leaf wall with cobblestone and mortar infill under out-of-plane loading. The example aims to investigate the seismic resistance of this type of structural component in the weak out-of-plane direction. The above example has been modelled with the numerical strategy proposed here, and the results have been compared with previous numerical outcomes obtained by limit and FE analysis, as reported in [6].

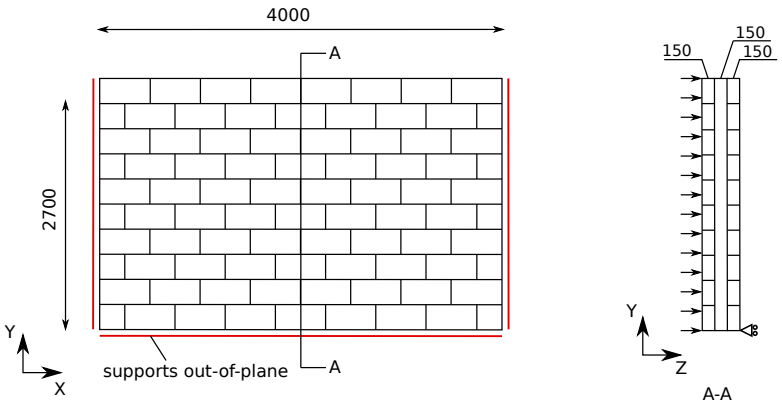

Figure 20. Front view and cross-section of multi-leaf wall with sketch of boundary conditions.

As shown in Figure 20 (a), the width of the wall is 4.0m, and the height is 2.7m, while the thickness of the layers is 0.15+0.15+0.15m. The two masonry panels consist of brick masonry in simple running bond arrangement. The wall is restrained along the bottom and the side edges at the level of the extrados, forming pinned supports. The bottom surface of the wall is connected to the fully restrained "ground" through interface elements representing the frictional interaction

DOI: 10.1002/nme

along this frictional interface. A uniformly distributed force load has then been applied over the intrados pointing towards the wall. Dynamic analysis has been performed with the load applied quasi-statically.

Table V. Material parameters of brick-masonry in multi-leaf wall.

Bricks	Elastic modulus $E_b(N/mm^2)$	Poisson's ratio ν_b	Unit weight $\rho_b(kN/m^3)$
	30000	0.15	21.3
Brick-mortar interface	Tensile strength $\sigma_{t0}(N/mm^2)$	Cohesion $c_i(N/mm^2)$	Friction angle ϕ_0
	0.32	0.384	30^o
	Fracture energy $G_{fI}(N/mm)$	Fracture energy $G_{fII}(N/mm)$	
	0.01	0.05	

In the present work, the masonry panels have been modelled with a mesoscale description of the running bond using 2 solid elements per brick unit, while the infill material domain has been modelled independently with a structured mesh of 15-noded wedge elements. The nonlinear material behaviour of the infill has been described with a Drucker-Prager constitutive law. The material properties used for the brick masonry are reported in Table V, while those used for the infill material are listed in Table VI. Some of those values - mainly the strength parameters - were provided in [6], as they correspond to parameters used in limit analysis. The remaining parameters reported in Tables V and Table VI are chosen based on average values for similar materials. Concerning the elastic stiffness of the material models, a range of different possible values has been considered to investigate the influence of the elastic properties on the ultimate load.

Table VI. Material properties of infill material in multi-leaf wall.

Cohesion $c_f(N/mm^2))$	Friction angle ϕ_f	Poisson's ratio ν_f	Unit weight $\rho_f(kN/m^3)$
0.117	25^o	0.20	19.1

Initially, the domain of the infill material has been modelled with three different levels of refinement to test the influence in the results and verify the efficiency of the coupling method along the non-conforming interface. The finer and coarser meshes are shown in Figures 21 (a) and (b) respectively. The global nonlinear behaviour of the structure is identical for the different meshes, as shown in Figure 20 (b). In these analyses the elastic stiffness of the mortar joints is taken equal to $E_m = 2000N/mm^3$ and the Young's modulus of the infill material equal to $E_i = 1000N/mm^2$. The plots trace the displacement u_z at the top of the wall at mid-width and mid-thickness against the surface load. After reaching the peak load, the displacements increase continuously without change in the load level, as dynamic analysis was performed under force control.

Subsequently, using the most computationally efficient discretisation of *'model 6x10x1'* for the infill domain, the coupled masonry panel has been analysed for a range of values of the elastic parameters of the constituents. The limit analysis does not require elastic parameters, since it is only concerned with the limit state where the collapse mechanism is developed and it aims at providing an upper bound of the ultimate load. As shown in Figure 22, all the predicted peak loads are below the value provided by limit analysis, therefore the upper bound is confirmed. However, a notable variation of the peak loads can be observed, depending on the elastic parameters of the materials.

For low - still within realistic limits - values of the elastic parameters, the peak load can be significantly lower than the upper limit. The values tend to stabilise close to the upper limit for stiff materials. This observation is consistent with what would be expected theoretically. The elastic characteristics of the materials influence the distribution of the inelastic strains that are produced

DOI: 10.1002/nme

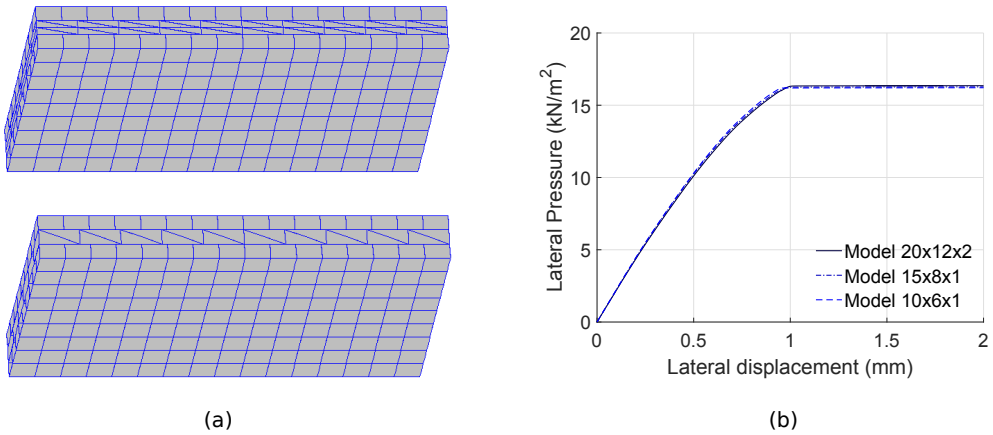

Figure 21. (a) Models with different meshes for the infill domain: $20 \times 12 \times 2$ mesh (top) and $10 \times 6 \times 1$ mesh (bottom); ; (b) Global out-of-plane response of multi-leaf wall for different levels of infill mesh refinement.

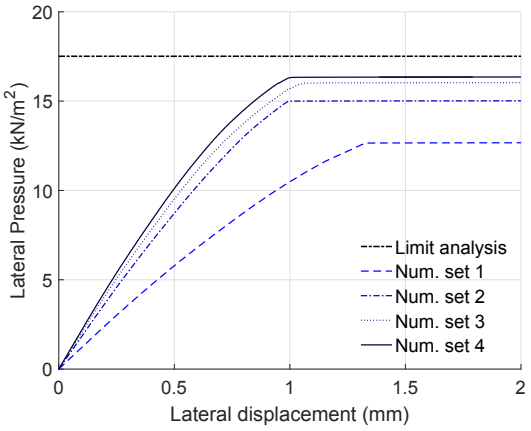

Set	Joint elastic stiffness [N/mm^3]		Infill elastic stiffness [N/mm^2]
1	Kn=50	Kt=30	Ei=500
2	Kn=100	Kt=50	Ei=800
3	Kn=200	Kt=100	Ei=1000
4	Kn=500	Kt=300	Ei=2000

Figure 22. Global behaviour of multi-leaf wall under out-of-plane loading for different values of elastic stiffness parameters.

during the analysis. When using softening material models, the distribution of the inelastic strains influences the distribution and measure of the stresses and consequently it can have an influence in the ultimate strength of the structure. This effect is more pronounced for small elastic stiffness, as in this case the change in the inelastic strain distribution is larger. The above observations confirm one of the advantages of the sophisticated FE modelling with softening material behaviour for capturing details of the response of coupled structures.

With respect to the cracking pattern, it consists of two diagonal cracks from the middle of the top surface to the bottom edges, as shown in Figure 23. The pattern for the higher elastic stiffness values coincide with the failure pattern reported in [6]. For lower values of the elastic parameters the position of the cracks shifts to a limited extend.

DOI: 10.1002/nme

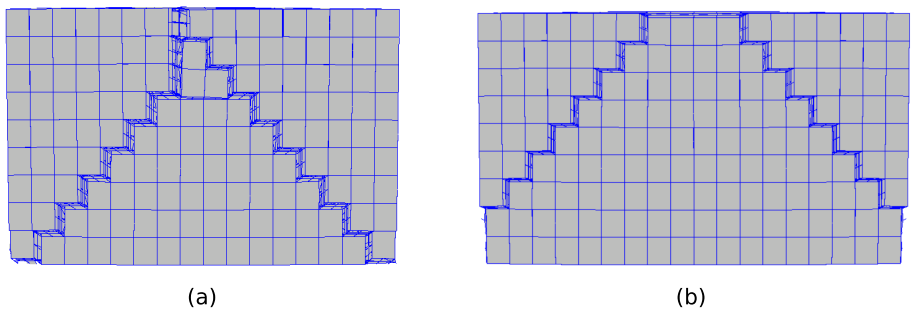

Figure 23. Cracking patterns of the multi-leaf wall under out-of-plane loading: (a) low elastic stiffness, (b) high elastic stiffness.

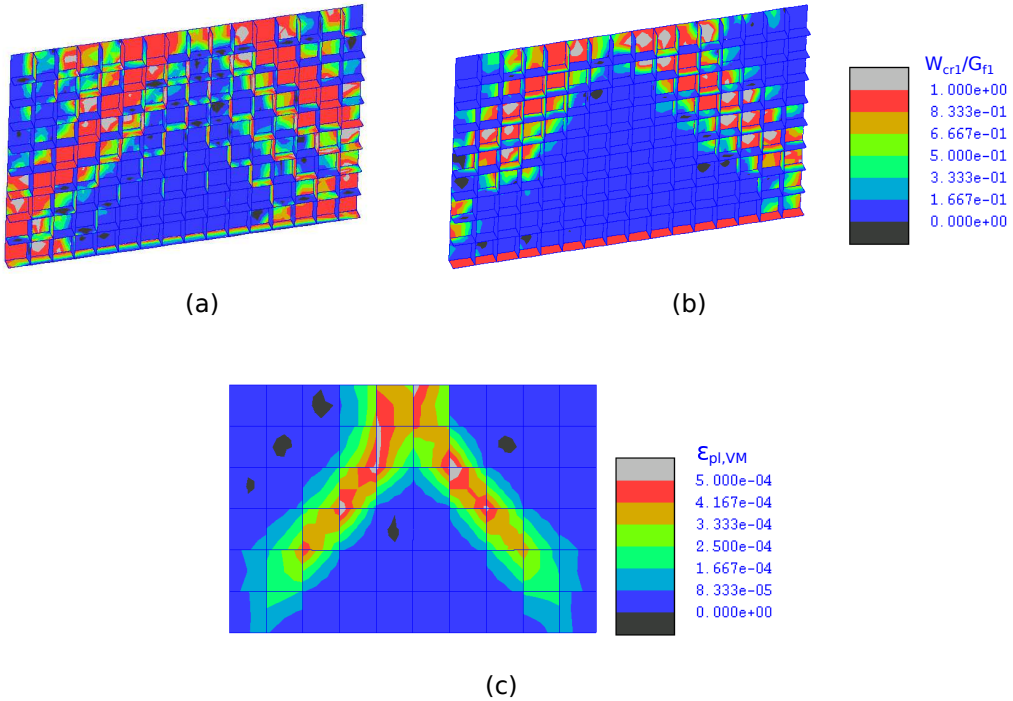

Figure 24. Plastic work developed in the interfaces of: (a) the extrados masonry panel and (b) the intrados masonry panel at the maximum load; (c) Plastic deformation developed in the infill material at the maximum load.

5. CONCLUSION

This work proposes an advanced partitioned mesoscale strategy for coupled masonry structures. The URM parts are modelled in mesoscale, ensuring an accurate representation of their in-plane and out-of-plane nonlinear behaviour, while other material components are represented with continuous meshes. A 3D non-conforming mesh tying method is developed for the coupling of the individual meshes. As a result, each structural component can be modelled independently, which allows the flexible 3D modelling of complex heterogeneous structures with URM components. The modelling

DOI: 10.1002/nme

of such structures using mesoscale descriptions of the URM parts would be cumbersome or even impossible if mesh compatibility was required.

Furthermore, zero-thickness cohesive interface elements are employed for the realistic representation of the physical behaviour of the coupling interfaces. Thus on the whole, the proposed strategy accurately accounts for both the nonlinear behaviour of each component and the nonlinear interaction between them.

The generally increased computational cost typically associated to the analysis of these detailed models is addressed through i) the optimisation of the continuous meshes enabled by the elimination of the mesh compatibility requirement and ii) the use of hierarchic domain partitioning and parallel computing.

The proposed strategy results in accurate response predictions, as demonstrated by the comparison of numerical results with existing experimental and numerical outcomes. Importantly, the proposed 3D coupled modelling approach captures characteristics of the structural response that cannot be represented with more simplified approaches, thus allowing the investigation of heterogeneous URM systems at an unprecedented level of sophistication, and offering valuable insight into their typically complex response.

ACKNOWLEDGEMENTS

The first author would like to acknowledge the financial support of the President's PhD Scholarships of Imperial College London. Additionally, the authors acknowledge the support of the HPC Service of Imperial College London for the computational resources provided for the numerical analyses performed here. Finally, the authors would like to thank Prof. G. Milani for the details he has provided on the numerical example presented in Section 4.2.

REFERENCES

1. Hughes TG, Blackler MJ. A review of the uk masonry arch assessment methods. *Proceedings of the Institution of Civil Engineers. Structures and buildings* 1997; **122**(3):305–315.
2. Egermann R. Investigations on the load bearing behaviour of multiple leaf masonry. *IABSE REPORTS* 1993; :305–305.
3. Cavicchi A, Gambarotta L. Collapse analysis of masonry bridges taking into account arch–fill interaction. *Engineering Structures* 2005; **27**(4):605–615.
4. Gilbert M. Limit analysis applied to masonry arch bridges: state-of-the-art and recent developments. *5th International Arch Bridges Conference*, 2007; 13–28.
5. Grande E, Milani G, Sacco E. Modelling and analysis of frp-strengthened masonry panels. *Engineering Structures* 2008; **30**(7):1842–1860.
6. Milani G. 3d fe limit analysis model for multi-layer masonry structures reinforced with frp strips. *International Journal of Mechanical Sciences* 2010; **52**(6):784–803.
7. Fanning PJ, Boothby TE. Three-dimensional modelling and full-scale testing of stone arch bridges. *Computers & Structures* 2001; **79**(29):2645–2662.
8. Binda L, Pina-Henriques J, Anzani A, Fontana A, Lourenço PB. A contribution for the understanding of load-transfer mechanisms in multi-leaf masonry walls: Testing and modelling. *Engineering Structures* 2006; **28**(8):1132–1148.
9. de Felice G. Assessment of the load-carrying capacity of multi-span masonry arch bridges using fibre beam elements. *Engineering Structures* 2009; **31**(8):1634–1647.
10. Pelà L, Aprile A, Benedetti A. Comparison of seismic assessment procedures for masonry arch bridges. *Construction and Building Materials* 2013; **38**:381–394.
11. Betti M, Drosopoulos GA, Stavroulakis GE. Two non-linear finite element models developed for the assessment of failure of masonry arches. *Comptes Rendus Mécanique* 2008; **336**(1-2):42–53.
12. Thavalingam A, Bicanic N, Robinson JI, Ponniah DA. Computational framework for discontinuous modelling of masonry arch bridges. *Computers & structures* 2001; **79**(19):1821–1830.
13. Milani G, Lourenço PB. 3d non-linear behavior of masonry arch bridges. *Computers & Structures* 2012; **110**:133–150.
14. Zhang Y. Advanced nonlinear analysis of masonry arch bridges. PhD Thesis, Imperial College, University of London 2014.
15. Macorini L, Izzuddin BA. A non-linear interface element for 3d mesoscale analysis of brick-masonry structures. *International Journal for numerical methods in Engineering* 2011; **85**(12):1584–1608.
16. Jokhio GA, Izzuddin BA. A dual super-element domain decomposition approach for parallel nonlinear finite element analysis. *International Journal for Computational Methods in Engineering Science and Mechanics* 2015; **16**(3):188–212.
17. Macorini L, Izzuddin BA. Nonlinear analysis of masonry structures using mesoscale partitioned modelling. *Advances in engineering Software* 2013; **60**:58–69.

18. Izzuddin BA. An enhanced co-rotational approach for large displacement analysis of plates. *International Journal for Numerical Methods in Engineering* 2005; **64**(10):1350–1374.
19. Jokhio GA. Mixed dimensional hierarchic partitioned analysis of nonlinear structural systems. PhD Thesis, Imperial College, University of London 2012.
20. Unger JF, Eckardt S. Multiscale modeling of concrete. *Archives of Computational Methods in Engineering* 2011; **18**(3):341–393.
21. Papadopoulos P, Taylor RL. A mixed formulation for the finite element solution of contact problems. *Computer Methods in Applied Mechanics and Engineering* 1992; **94**(3):373–389.
22. Aminpour MA, Ransom JB, McCleary SL. A coupled analysis method for structures with independently modelled finite element subdomains. *International Journal for Numerical Methods in Engineering* 1995; **38**(21):3695–3718.
23. Laursen TA, Heinstein MW. Consistent mesh tying methods for topologically distinct discretized surfaces in non-linear solid mechanics. *International journal for numerical methods in engineering* 2003; **57**(9):1197–1242.
24. Park KC, Felippa CA, Rebel G. A simple algorithm for localized construction of non-matching structural interfaces. *International Journal for Numerical Methods in Engineering* 2002; **53**(9):2117–2142.
25. Puso MA. A 3d mortar method for solid mechanics. *International Journal for Numerical Methods in Engineering* 2004; **59**(3):315–336.
26. Dohrmann CR, Key SW, Heinstein MW. Methods for connecting dissimilar three-dimensional finite element meshes. *International Journal for Numerical Methods in Engineering* 2000; **47**(5):1057–1080.
27. Ben Belgacem F, Maday Y. The mortar element method for three dimensional finite elements. *RAIRO-Modélisation mathématique et analyse numérique* 1997; **31**(2):289–302.
28. Puso MA, Laursen TA. Mesh tying on curved interfaces in 3d. *Engineering Computations* 2003; **20**(3):305–319.
29. Flemisch B, Wohlmuth BI. Stable lagrange multipliers for quadrilateral meshes of curved interfaces in 3d. *Computer Methods in Applied Mechanics and Engineering* 2007; **196**(8):1589–1602.
30. *ABAQUS/Standard User's Manual, Version 6.14*. Simulia, 2014.
31. Becker R, Hansbo P, Stenberg R. A finite element method for domain decomposition with non-matching grids. *ESAIM: Mathematical Modelling and Numerical Analysis* 2003; **37**(2):209–225.
32. Kim HG. Development of three-dimensional interface elements for coupling of non-matching hexahedral meshes. *Computer Methods in Applied Mechanics and Engineering* 2008; **197**(45):3870–3882.
33. Irons BM. A frontal solution program for finite element analysis. *International Journal for Numerical Methods in Engineering* 1970; **2**(1):5–32.
34. Simo JC, Laursen TA. An augmented lagrangian treatment of contact problems involving friction. *Computers & Structures* 1992; **42**(1):97–116.
35. Izzuddin BA. Nonlinear dynamic analysis of framed structures. PhD Thesis, Imperial College, University of London 1991.
36. Melbourne C, Gilbert M. The behaviour of multiring brickwork arch bridges. *Structural Engineer* 1995; **73**(3).
37. Adibaskoro T. Nonlinear simulations of masonry arch bridges. Master's Thesis, Imperial College, University of London 2015.